Spin State Manipulation of Spiropyran (SP) and Dy Complex with SP Ligand Molecules on Au (111) by Scanning Tunneling Microscopy

Jie Hou, Dongzhe Li, Lucie Norel, Stéphane Rigaut, Zhipeng Wang, Lei Shan, Tadahiro Komeda

View Article Online
DOI: 10.1039/D3TC02513F

Spin State Manipulation of Spiropyran (SP) and Dy Complex with SP Ligand Molecules on Au (111) by Scanning Tunneling Microscopy

Jie Hou[1], Dongzhe Li[2], Lucie Norel[3], Stéphane Rigaut[3], Zhipeng Wang[4], Lei Shan[1], Tadahiro Komeda[4,5*]*

[1]Key Laboratory of Structure and Functional Regulation of Hybrid Materials of Ministry of Education, Institutes of Physical Science and Information Technology, Anhui University, Hefei 230601, China

[2]CEMES, Université de Toulouse, CNRS, 29 rue Jeanne Marvig, F-31055 Toulouse, France

[3]Institute of Chemical Sciences of Rennes (ISCR), UMR 6226 CNRS, University of Rennes 1, Rennes Cedex, France

[4]Institute of Multidisciplinary Research for Advanced Materials (IMRAM, Tagen), Tohoku University, 2-1-1, Katahira, Aoba-Ku, Sendai 980-0877, Japan

[5]Center for Spintronics Research Network, Tohoku University, 2-1-1 Katahira, Aoba-ku, Sendai 980-8577, Japan

View Article Online
DOI: 10.1039/D3TC02513F

Abstract: We examine the isomerization and the variation of the spin state of molecules adsorbed on Au (111) surface by injecting tunneling electrons. We employed molecules of spiropyran (SP) and SP-based Dy complex with hexa-fluoro-acetylacetonate (hfac) ligand and DyN_3O_5 coordination (SP-DyL(hfac)$_2$). SP molecules, transferred by vacuum sublimation, form an ordered lattice. Injection of tunneling electrons changes the conformation of the SP molecule, which can be accounted for by an isomerization into a merocyanine (MC) molecule. The change of the magnetic property is confirmed by detecting the Kondo resonance, which is a high-density of states at the Fermi level by forming the spin-singlet in the neighbor of the spin impurity. The appearance of the Kondo resonance is detected only in the converted MC molecule, which originated from the MC molecule's π radical. Tunneling electrons injection can cause a similar isomerization for the SP-DyL(hfac)$_2$ molecule. The appearance of the magnetic moment is detected after the conversion by the Kondo resonance, which suggests the formation of MC-DyL(hfac)$_2$. Density functional theory calculations support experimental observations. Since the MC-DyL(hfac)$_2$ molecule's single-molecule magnet nature was confirmed previously, this report's observation might pave the way for designing and developing single-molecule magnets based on photoisomerization.

Keywords: spiropyran; merocyanine; Kondo resonance; scanning tunneling microscopy and spectroscopy, density functional theory

View Article Online
DOI: 10.1039/D3TC02513F

Introduction

With the ever-increasing demand for ultra-capacity storage media, researchers are attempting to shrink data storage to achieve as large a storage capacity in as small a space as possible[1]. Research on utilizing molecules to encode information and improve efficiency has recently attracted attention[2-4]. Photochromic molecules have been identified as a novel type of molecular spin qubit[5] since they can be reversibly interconverted between two conformational isomers with external stimuli such as light, temperature, pressure, and so forth[6]. The two distinct conformations represent two states corresponding to "0" and "1" in binary[7]. Therefore, such molecules can be used as qubits to store and process quantum information.

Up to now, significant efforts have been made regarding how to tune and realize the reversible isomerization for photochromic complexes[6]. In contrast to the conventional approaches, scanning tunneling microscopy and spectroscopy (STM/STS) is an intriguing tool for precisely controlling such conformation isomerization since it can inject tunneling electrons with high spatial and energy resolution[8, 9]. The development of the "atomic manipulation" technique continues to reveal nanoscale phenomena[10-12]. At the same time, the tunneling electrons could interact with the local magnetic moment and reveal abundant phenomena associated with spin-flip dynamics, such as Kondo resonance[9]. The sign of the Kondo state is a sharp renormalized quasi-particle peak near the Fermi level. Therefore, researchers could indirectly investigate the spin state of adsorbate magnetic atoms or molecules by detecting such resonance[13-15].

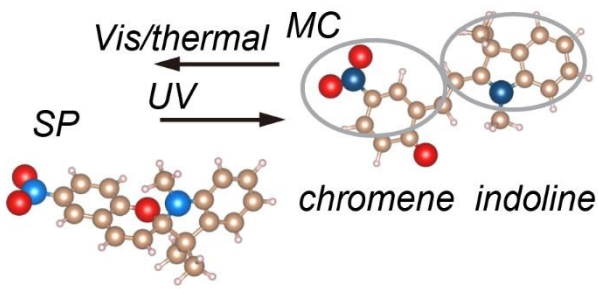

Fig. 1 Schematic of isomerization between SP and MC.

Among photochromic molecules, spiropyran (SP) is a promising candidate as it can be readily converted to isomeric merocyanine (MC) form accompanying significant changes both in structure and electronic properties[16], as sketched in **Fig. 1**[6]. Meanwhile,

View Article Online
DOI: 10.1039/D3TC02513F

combining photochromic SP and magnetic anisotropy of 4*f* metal ions can produce functionalized single-molecule magnets (SMMs) with intriguing photo responsive features[17-19]. Recently, Paquette and coworkers observed the photoinduced change of the coordination environment of lanthanide ions by a photo-isomerization of spiropyran and spirooxazine ligands[18, 19]. Such isomerization reveals that lanthanide compounds based on SP are candidates for the modulation of photoelectric and photomagnetic properties since the isomerization of SP to MC is expected to result in significant changes in the lanthanide ion environment. Toward this end, we previously employed bis(2-pyridinemethyl)amine and 8-(iodomethyl) spirobenzopyran as sources to synthesize the chelating SP ligand (L_{SP}), which has strong coordination with Ln^{III} ions[17]. In the presence of sodium iodide, L_{SP} can react with one equivalent of $M(hfac)_3 \bullet 2H_2O$ (M = Dy, hfac = hexa-fluoro-acetylacetonate) and form a molecule containing hfac ligand whose coordination is similar to ($MC\text{-}DyN_3O_5$)[17]. The structure is sketched in our previous publication[17]. Hereafter, in this work, we express this molecule as MC-DyL$(hfac)_2$ and prepare SP-DyL$(hfac)_2$. Such isomerization provides highly charged phenolic oxygen. Combining the oxygen from phenolate and the less-charged nitrogen atoms from bis(2-pyridinemethyl)amine moiety creates a solid axial magnetic anisotropy in DyL$(hfac)_2$. As a result of the high magnetic anisotropy of DyL$(hfac)_2$, the magnetic hysteresis loop shows a significant opening below 2 K, demonstrating a suitable SMM property[17].

In the present work, we focus on the conformation transformation of SP to MC and SP-DyL$(hfac)_2$ to MC-DyL$(hfac)_2$ by injecting tunneling electrons with an STM tip. The two converting processes are confirmed by detecting the Kondo resonance of the radical form of MC and MC-DyL$(hfac)_2$. The appearance of the Kondo peak reveals that the MC and MC-DyL$(hfac)_2$ are formed successfully by injecting tunneling electrons with the STM tip. Since the MC-DyL$(hfac)_2$ molecule's single-molecule magnet nature was confirmed previously, this report's observation might pave the way for designing and developing single-molecule magnets based on photoisomerization.

Methodology

A. Experiment

The experiment was performed under an ultra-high vacuum (UHV) system with a base pressure of less than 2×10^{-10} mbar, except for the drop-cast process. The clean Au (111) surface with a typical herringbone reconstruction pattern was prepared by

View Article Online
DOI: 10.1039/D3TC02513F

successive Ar^+ sputtering and annealing. SP is the commercial one (Aldrich), and MC-DyL(hfac)$_2$ molecules were synthesized following a previous recipe[6, 17].

To transfer the SP molecules onto Au (111), we use the vacuum sublimation technique from a homemade Ta boat heated at 280-300 °C after prolonged degassing. At the same time, the substrate is held at room temperature. The thickness and evaporation rate of the molecule were recorded with a quartz crystal microbalance (QCM) mounted on top of the preparation chamber. However, the MC-DyL(hfac)$_2$ molecule was transferred onto Au (111) with the drop-cast method in N_2 ambient, a part of which spontaneously isomerized to SP-DyL(hfac)$_2$ on the gold surface. The measurement was performed using a dilution refrigerator-based STM/STS at a base temperature of 4 K, as determined by a temperature sensor close to the STM head. STM topographies were obtained in constant current mode, and the *dI/dV* spectra of Kondo resonance were taken using a lock-in amplifier with a sinusoidal modulation voltage of V_{rms} = 1 mV (room-mean square value), and frequency of f_{mod} = 475 Hz were superimposed onto the bias voltage.

B. Calculations

For structure optimization and molecular orbital estimation, we employ the VASP code, a plane wave basis set and PAW potentials to describe the behavior of the valence electrons[20-22]. A generalized gradient Perdew-Burke-Ernzerhof (PBE) exchange-correlation potential[23] was used. The structures were relaxed until the forces were smaller than 0.05 eV/Å.

The detail of the molecules' magnetic properties is calculated using spin-polarized *ab initio* calculations in which the plane wave electronic structure package Quantum ESPRESSO[24] in the density functional theory (DFT) framework. The B3LYP[25] hybrid function was used for the exchange-correlation function within the ultra-soft pseudopotential formalism. Energy cut-offs of 30 Ry and 300 Ry were employed for the wave function and the charge density, respectively.

View Article Online
DOI: 10.1039/D3TC02513F

Results and Discussion

We transfer the samples onto the Au (111) substrate. Since the Au (111) surface is more chemically inert and provides a weak interaction with adsorbed molecules compared with Ag (111) and Cu (111) surfaces, it can preserve the original configuration of organic radicals[8, 26]. **Fig. 2** shows the STM images of the Au (111) surface after transferring the SP molecules by a vacuum sublimation method. In **Fig. 2(a)**, a well-ordered film of SP on Au (111) substrate is illustrated, where a lattice of the molecular film with a characteristic herringbone structure of the underlying Au (111) is visible. The high-resolution STM topographic image with a sample bias (V_s) of −0.6 eV is shown in **Fig. 2(b)**. An intra-molecule contrast variation (high and low parts) is visible in a single molecule, which is illustrated as a combination of the circle (high) and bar (low) in the upper-left corner of the image (mark I). A magnified STM image for a single molecule is shown in **Fig. 2(c)**. Interestingly, the neighbor molecule marked by II has a similar contrast variation, but the direction is reversed from molecule I. The molecule axis is aligned in the $[\mathbf{1\bar{1}0}]$ direction, along which direction molecules make a chain with an identical intra-molecular direction. The molecules are directed to opposite directions on the neighboring chain (next chain in the $[\mathbf{11\bar{2}}]$ direction). A similar phenomenon was reported in previous observations[27, 28]. The periodicity of the lattice of the SP film is 1.44 and 1.25 nm in $[\mathbf{1\bar{1}0}]$ and $[\mathbf{11\bar{2}}]$ directions, respectively. We expect that a hydrogen bond is formed between the molecules in the row, forming tail-and-head bonding. Hydrogen bonding should be the dominant intermolecular interaction for forming the self-assembled pattern[29].

The unit cell is expressed as a white rectangle with two vectors ***s*** and ***t***, which are orthogonal to each other and with a length of 5 a and 4.3a, respectively (a ~ 0.288 nm, nearest neighbor distance of Au (111) surface). The lattice and the intra-molecule topographic STM image are sketched in **Fig. 2(d)** with Au (111) substrate shown by yellow circles. The longer vector ***s*** is along the close-packed direction of $[\mathbf{1\bar{1}0}]$ of Au (111) surface. Even though the unit cell of such size means that the self-assembled SP network is slightly incommensurate with the Au (111) surface, the experimentally observed lattice of SP film is comparable to the previous report[29].

View Article Online
DOI: 10.1039/D3TC02513F

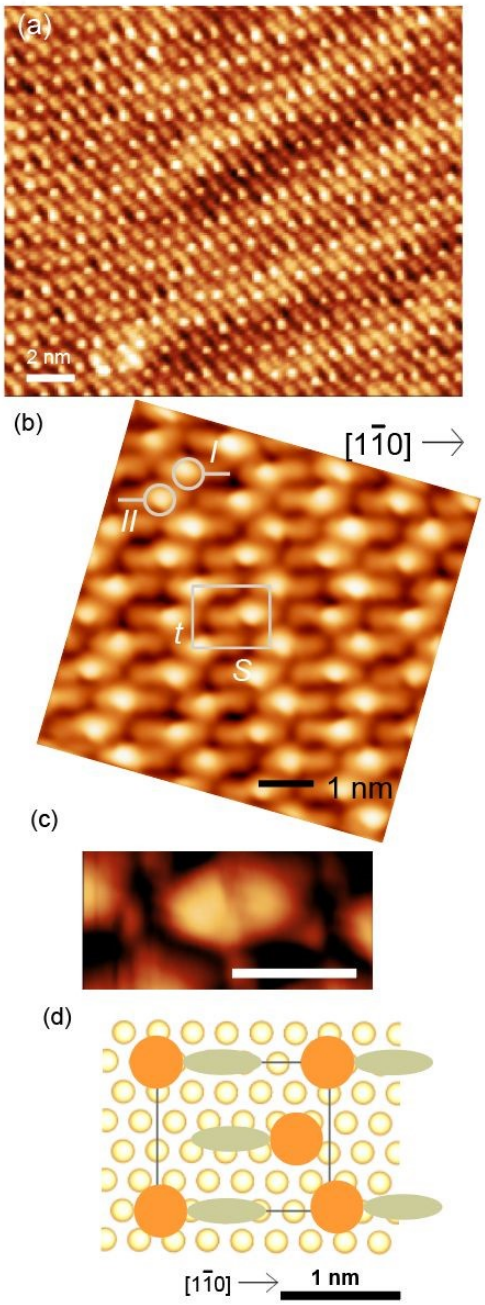

Fig. 2 (a) STM topographic image of SP molecule film on Au (111) formed by a thermal sublimation. (b), (c) Magnified STM image of the SP film, (b), and the molecule, (c). A circle-and-bar in the upper left illustrates the schematic distribution of height variation in a single molecule, where I and II direct opposite directions. Rectangle with **s** and **t** vectors represent the unit cell of the film, containing two molecules. Length scales of (b) and (c) are 1 nm. ($V_s = -0.6$ V, $I_t = 92$ pA). (d) Schematics of the molecule lattice and the height distribution (corresponding to I and II of (b)). Au substrate is shown by yellow balls, and the $[1\bar{1}0]$ direction is aligned with the horizontal direction.

View Article Online
DOI: 10.1039/D3TC02513F

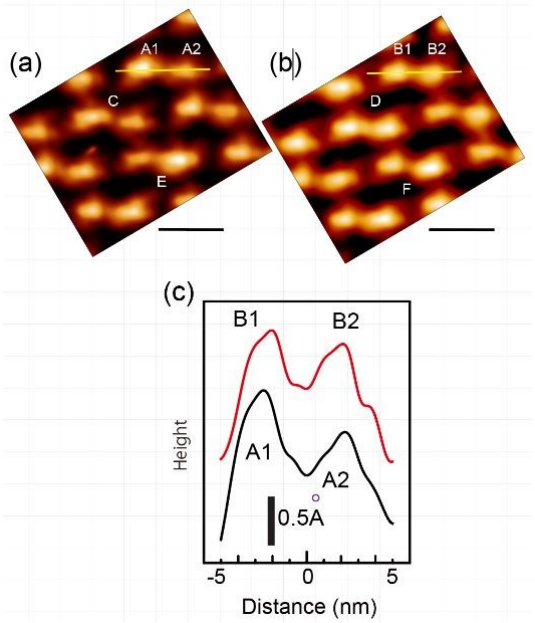

Fig. 3 (a), (b) Before (a) and after (b) the electron injection at the SP molecule film. The tip was positioned at the molecule's center, containing A1 (brighter) and A2 (darker) spots. The target molecule was changed into a molecule containing B1 and B2 with a similar height. A similar change occurs in the neighbor molecule (C →D), but there occurs no change for further separated molecules (no change in E→F) (Length scale = 1 nm, $V_s = -0.6$ V). (c) Line profile along A1-A2 and B1-B2 of (a) and (b), respectively.

It was demonstrated that the photochromic isomerization shown in **Fig. 1** can be realized with electron injection. We examined an electron injection effect on our SP film. The change of the STM image is shown in **Fig. 3(a)** and **(b)** for before and after electron injection, respectively. We inject tunneling electrons at the center of the single molecule containing A1 and A2, which change to B1 and B2. The height profile along the molecular axis is shown in **Fig. 3(c)**. There is a clear difference between A1 and A2; A1 is higher in height, and A2 is lower. After the electron injection (the sample bias of 2.0 eV and the current of 0.1 nA for 30-60 sec), the two parts of B1 and B2 have a similar height, evident in the height profile of **Fig. 3(c)**. The change is due to the difference in the heights of the two parts in the SP and MC molecules. They should be the result of the conversion of the molecule from the SP to MC states.

View Article Online
DOI: 10.1039/D3TC02513F

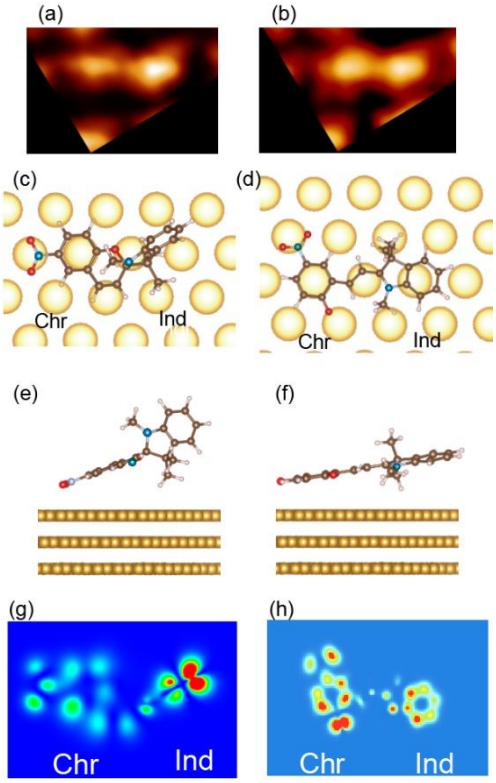

Fig. 4 (a), (b) Before, (a), and after, (b), the electron injection at the SP molecule film. A single molecule contains the two spots. (c)-(f) Optimized structure of the molecule structure and bonding on Au (111) using VASP code. (c), (d) ((e), (f)) correspond to top- and side-view of the SP (MC) molecule, respectively. (g), (h) STM simulation of the SP, (g), and MC, (h). Marks Chr and Ind mean chromene and indoline parts, respectively. The color code of the atoms in the molecule is the same as in **Fig. 1**.

We consider the SP and MC molecules' bonding configuration and simulate the electronic structures' for the STM images. As shown in **Fig. 1(a)**, SP and MC molecules are composed of the chromene part with the NO_2 moiety and the indoline part.

Due to the ring closing/opening, the planes of the two parts are perpendicular to each other in the SP state and parallel in the MC state. The target STM topographic images are shown in **Fig. 4(a)** and **(b)**; the former is SP, and the right part is higher than the left, while the latter is MC converted from **Fig. 4(a)** and has a similar height in the left and right parts.

For the SP molecule, we made an initial configuration in which the indoline plane is upright and the chromene plane is relatively flat-lying. This configuration can make the NO_2 moiety bond with the substrate. We expect higher bonding energy with this

View Article Online
DOI: 10.1039/D3TC02513F

configuration, and a similar configuration is proposed in the previous report. On the other hand, the MC molecule is relatively flat, and we made a starting configuration close to a flat-lying one.

We execute the structural optimization with VASP starting from these configurations for both molecules. The most stable configurations are illustrated in **Fig. 4,** obtained after the optimization. For the SP molecule, the indoline part is upright to the surface. For the MC, the chromene and the indoline are close to the flat-lying condition. After calculating the electronic structure, we formed STM simulation images by slicing the charge distribution volume data with a plane parallel to Au (111) surface. The results are illustrated in **Fig. 4(g)** and **(h)** for SP and MC, respectively. The SP molecule has an enhanced charge density at the upright indoline part compared to the flat chromene part. The distribution changes when the SP changes to the MC molecule, in which the two parts have a similar charge density. We consider that the change from **Fig. 4(g)** to **(h)** corresponds to the image change from (a) to (b), reproducing the SP to MC conversion well.

View Article Online
DOI: 10.1039/D3TC02513F

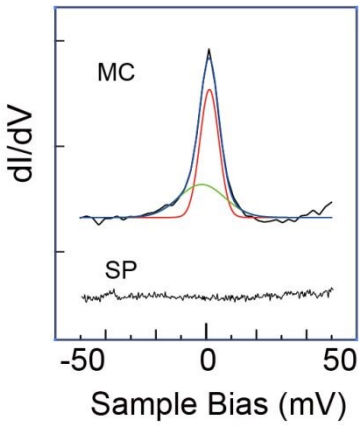

Fig. 5 STS spectra obtained for the molecules of SP and MC. Before opening the feedback loop, the tip was positioned at the set point V_s = −50 mV, I_t = 50 pA. A modulation of V_{rms} = 1 mV was superimposed on the sample bias for the lock-in amp detection. The solid lines show the fitting results (see main text).

The conversion from the SP molecule to the MC molecule appears more clearly in the magnetic property. The appearance of a magnetic moment when the SP molecule is converted into the MC molecule was investigated by electron spin resonance (ESR) experiment[30]. Detecting the Kondo resonance, the spin singlet state formed by screening an isolated spin by the itinerant electrons[31, 32], is a relatively straightforward method to detect an isolated spin. We see many examples of magnetic adsorbates detected by the Kondo resonance[9, 33-38].

The spectrum in the energy region near the Fermi level before and after the electron injection is shown in **Fig. 5**. The spectrum obtained for the SP molecule offers no feature. However, the one after the electron injection contains a sharp feature at the Fermi level. By measuring the temperature dependence of this peak, we conclude that it is a Kondo resonance (see **Figure S2** of Supporting Information).

The *dI/dV* spectra can be well fitted by the Fano function[34, 39]

$$\frac{dI}{dV} = a\frac{(\varepsilon + q)^2}{1+\varepsilon^2} + b; \qquad \varepsilon = \frac{eV - \varepsilon_0}{\Gamma}$$

where $\boldsymbol{q}$ is the Fano asymmetry parameter, $\boldsymbol{\varepsilon_0}$ is the energy shift of the resonance from the Fermi level; $\boldsymbol{\Gamma}$ is the half-width at half maximum; $\boldsymbol{a}$ is the amplitude coefficient; $\boldsymbol{b}$ is the background conductance signal[40, 41]. The fitting parameters are q=−100.42 ± 0.86 and Γ= 6.2 mV. The large $\boldsymbol{q}$ corresponds to where most tunneling electrons pass through the

View Article Online
DOI: 10.1039/D3TC02513F

molecule rather than the substrate, suggesting a weak interaction between the MC and Au (111).

The red curve in the deconvoluted fitting of **Fig. 5** shows the principal component discussed above, while a broader side peak appears on the negative energy side, plotted by a green line. A similar side peak was observed by our group and is assigned to the phonon excitation in the inelastic tunneling process[38]. Since the conversion occurs with a slow bias ramping, we exclude the possibility of the electric field for the isomerization mechanism. The conversion mechanism is discussed for the solution case[42]. In solution, it has been demonstrated that SP and MC are two stable states and can be switched: SP to MC by UV irradiation and MC to SP by visible light or by thermal heating. Energetically, SP is more stable than MC, the latter in the trans-MC state, and the cis-MC is in the transition state[42]. The energy diagram is shown in **Figure S1** of Supporting Information. We consider that the tunneling electrons we injected for the molecule's conversion provide this energy, which makes the conversion from SP to MC.

View Article Online
DOI: 10.1039/D3TC02513F

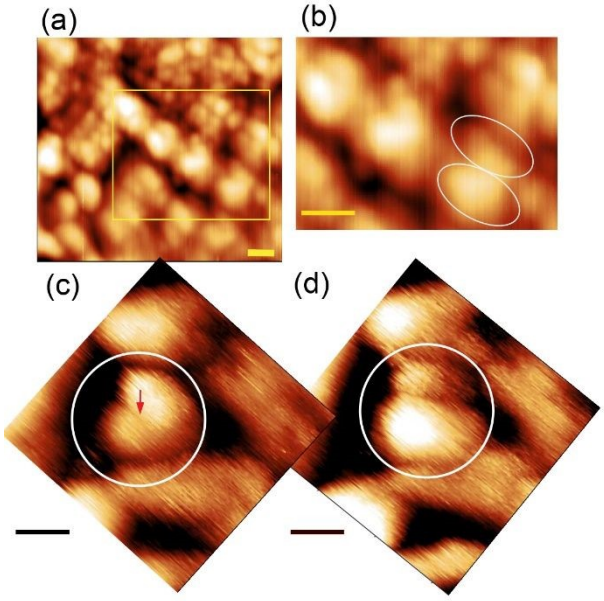

Fig. 6 (a) (b) STM images of Au (111) surface after SP-DyL(hfac)$_2$ molecules transferred by a drop cast method ($V_s = -1.0$ V, $I_t = 60$ pA, length scale =1 nm). Four molecules are aligned in a line inside the white square (a), magnified in (b). Elongated circles represent two distinct bright regions in a molecule separated by a node. (c) (d) Before, (c), and after, (d), the electron injection onto a center molecule. The circles and the arrows in (c) and (d) indicate the target molecule and the position of the electron injection, respectively. Observation conditions and length scales are identical with (a) and (b).

Next, we discuss the observation and electron injection for the SP-DyL(hfac)$_2$ molecule. As we stated in the introduction, a molecule Dy complex containing two hfac and SP (MC) ligands is called SP-DyL(hfac)$_2$ (MC-DyL(hfac)$_2$).

We transfer the MC-DyL(hfac)$_2$ molecule onto the Au (111) by a drop-cast method. The vacuum sublimation method can provide a molecule transfer with a better purity of the molecule. However, since there is a possibility of a thermal dissociation of the molecule due to the size of the SP-DyL(hfac)$_2$ molecule, we avoid the vacuum sublimation method. We drop a dew of solution of MC-DyL(hfac)$_2$ molecule in dichloromethane (16 μmol/l) on Au (111), which is cleaned in a UHV chamber before the drop-cast process in an N_2 environment. After drying with nitrogen gas, the sample is returned to the UHV and cooled for the STM/STS measurement.

The topographic image of the surface is shown in **Fig. 6(a)**. We can notice circular protrusions, showing a local periodic alignment with a separation of 1.5 nm. A white square in **Fig. 6(a)** marks an example. The area is magnified in **Fig. 6(b)**. We judge that

View Article Online
DOI: 10.1039/D3TC02513F

each molecule is composed of two circular protrusions with a node in the middle; two protrusions are marked by oval circles in **Fig. 6(b)**. We should examine the possibility that the ball-like features assigned to the target molecule are impurities originating from the solvent or dissociated species. The robustness of the molecule transferred by the drop cast method was examined by a time-of-flight secondary ion mass spectroscopy (ToF SIMS), which is described in SI. The target molecule dominates the species found on the surface, and we judge that the SP-DyL(hfac)$_2$ molecule is properly transferred onto Au (111) surface. Combined with the repetitive appearance of the identical features illustrated in **Fig. 6(a) and (b)**, we conclude that the ball-like features are the target molecule of SP-DyL(hfac)$_2$.

We then examined the tunneling electrons injection onto an SP-DyL(hfac)$_2$ molecule. The topographic image of the initial molecule is illustrated in **Fig. 6(c)**. A single molecule is marked by a circle in the figure, composed of two bright protrusions, and the lower one is slightly dimmer than the upper one. After the tunneling electron injection with a condition of V_s = 2.5 V, I_t = 0.1 nA, and 60 sec, the molecule changes to that observed in **Fig. 6(d)**. The tunneling voltage is changed from the observation condition (Vs = − 1.0 V) to Vs = 2.5 V slowly (ramping time of ∼10 sec) to avoid an unnecessary high electric field. The tip was positioned at the same place, keeping the feedback loop activated. After the electron injection, the lower protrusion becomes more enhanced than the upper one. This change is induced by the conversion of the SP part of the SP-DyL(hfac)$_2$ to MC-DyL(hfac)$_2$.

View Article Online
DOI: 10.1039/D3TC02513F

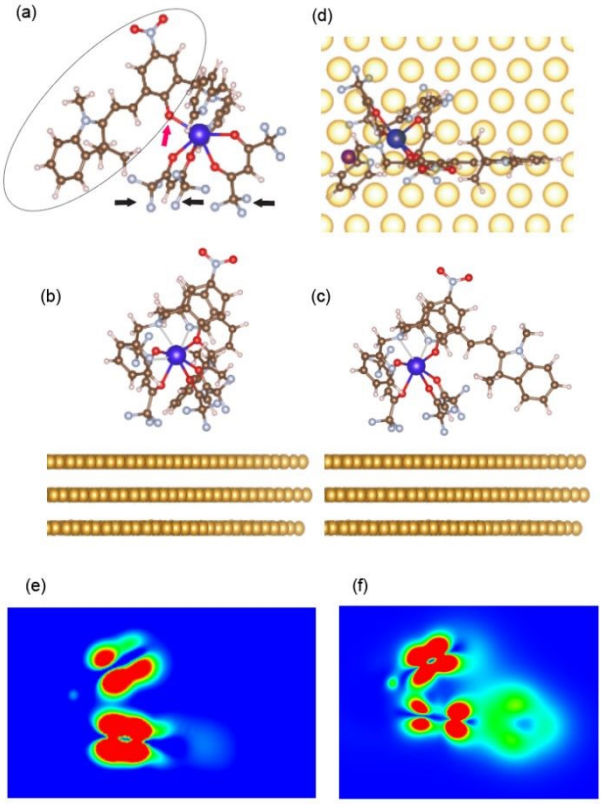

Fig. 7 (a) A schematic model of MC-DyL(hfac)$_2$. (b), (c) Side view of SP-DyL(hfac)$_2$, (b), and MC-DyL(hfac)$_2$, (c), and substrate Au (111) after a structural optimization by VASP. (d) Top view of (c). (e), (f) Simulated STM images for the structural optimized SP-DyL(hfac)$_2$ and MC-DyL(hfac)$_2$ adsorbed on Au (111).

We examine the structural models and bonding configurations of the SP- and MC-DyL(hfac)$_2$ molecules. The two molecules have a structure analog to DyN_3O_5, where the center Dy atom is coordinated by N and O atoms. The SP and MC molecules make a bond with the Dy atom by one O atom of the SP/MC species. The structure of the MC-DyL(hfac)$_2$ is illustrated in **Fig. 7(a),** in which the MC part is marked by an oval circle, and the oxygen atom attached to the Dy atom is marked by a red arrow. For the bonding configuration, we consider that the three CH_3 species denoted by the three black arrows attach to the Au (111) surface. This hypothesis is based on the following. First, the conversion from SP to MC is caused by the tunneling current. If the SP/MC part is attached to Au (111) surface, it is difficult to make the electrons injected into this part since other bulky ligands cover it. Second, the perimeters of the molecule other than the SP or MC part are terminated by CH and CH_3. The bonding by many legs of CH_3 can stabilize the bonding by gaining van der Waals energy, which makes the three-leg

View Article Online
DOI: 10.1039/D3TC02513F

bonding favorable. We then made a variety of initial bonding configurations and compared the bonding energies after structural optimization by VASP code.

The optimized structure for SP-DyL(hfac)$_2$ and MC-DyL(hfac)$_2$ are shown as side views in **Fig. 7(b)** and **(c)**, respectively. As we expected, the optimized structure of the two molecules is making a bond with Au (111) through the three CH_3 legs shown in **Fig. 7(a)**. The top view for the MC-DyL(hfac)$_2$ bonding configuration is illustrated in **Fig. 7(d)**. With the conversion from SP to MC, the indoline part is extended horizontally for the MC molecule compared to the SP-DyL(hfac)$_2$ due to the ring opening. At the same time, the density of the state at the top side of the molecule increases in the MC part. This is obvious in the simulated STM images of **Fig. 7(e)** and **(f)** for SP- and MC-DyL(hfac)$_2$, respectively. We found an enlarged DOS distribution for the latter case in the lower part of the image. We consider this can explain the contrast variation of the STM image of SP-DyL(hfac)$_2$ with the tunneling electron injection and conversion to MC, corresponding to the enhanced lower area of **Fig 6(d)**.

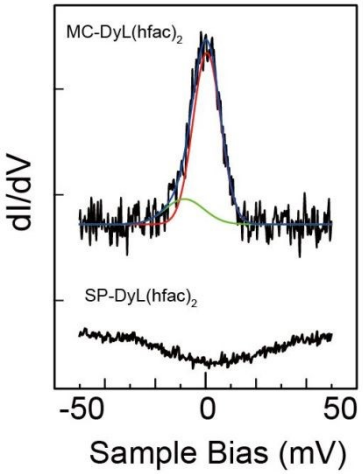

Fig. 8. STS spectra obtained for the molecules of SP-DyL(hfac)$_2$ (below) and the one after the electron injection, which is assumed MC-DyL(hfac)$_2$. Before opening the feedback loop, the set point was Vs = −50 mV, I_t = 50 pA, and the modulation of V_{rms} = 1 mV superimposed on the sample bias. The solid lines show the fitting results.

The isomerization from SP-DyL(hfac)$_2$ to MC-DyL(hfac)$_2$ appears more clearly in the Kondo resonance. The STS variation near the Fermi level before and after the electron injection on the drop-casted SP-DyL(hfac)$_2$ molecule is shown in **Fig. 8**. The appearance of the Kondo resonance after the electron injection supports the isomerization into the

View Article Online
DOI: 10.1039/D3TC02513F

MC-DyL(hfac)$_2$ molecule. We execute the Fano fitting as we did for the MC molecule. The fitting parameters are q=−35.03 ± 1.88, and I=10.0 mV. Red and green curves are the results of the deconvolution executed in a similar manner as we did in **Fig. 5**. The peak width, and hence the Kondo temperature, is ~ 1.5 times larger than that observed for the MC molecule. This might be related to the bonding of MC with the Dy atom in the MC-DyL(hfac)$_2$, but more detailed analysis is needed.

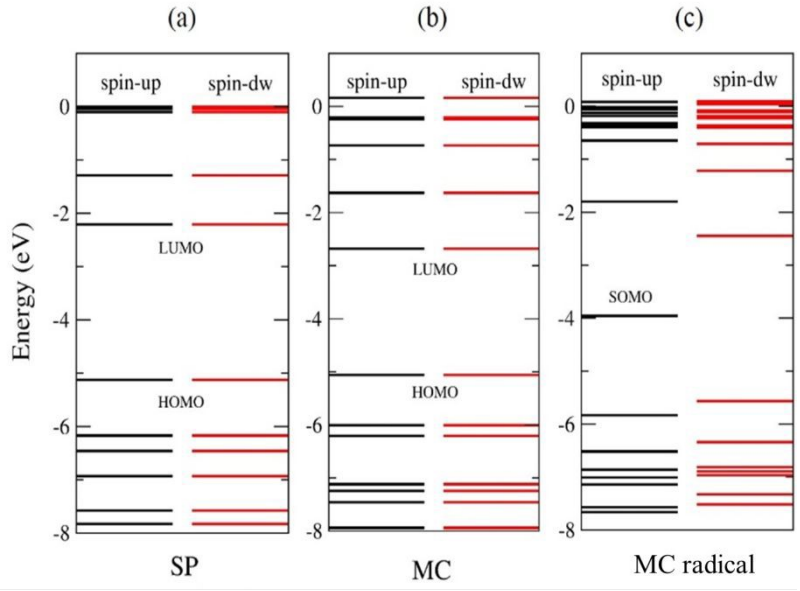

Fig. 9 DFT energy level diagram for SP (a), MC molecule (b), and MC radical (c) in the gas phase. Spin-up and spin-down (spin-dw) components are plotted in black and red lines.

To interpret the observed feature of Kondo resonance near the Fermi level, we compare the results of experimental observation with the calculated LDOS. **Fig. 9** shows the estimated energy level of SP, MC, and MC radical for spin-up and spin-down channels with B3LYP hybrid function[25]. SP in **Fig. 9 (a)** and MC in **Fig. 9 (b)** exhibit spin degeneracy with S=0, consistent with previous theoretical calculations[43]. Accordingly, no Kondo signal is expected from them.

While the MC radical is spin-polarized as shown in **Fig. 9 (c)**, the unpaired spin is mainly from the spin polarization between single occupied molecular orbital (SOMO) level of spin up and LUMO level of spin-down, which leads to S=1/2. The formation of the MC radical has been proposed in several references[16, 44]. Therefore, here we attribute the enhanced feature of the Kondo resonance to the SOMO orbital of the radical form of

View Article Online
DOI: 10.1039/D3TC02513F

MC and MC-DyL(hfac)$_2$. Meanwhile, the large gap (>1.5 eV) is also consistent with the stability of the Kondo effect after manipulation. In addition, it's known that the 4*f* spin can hardly mix with free electrons due to the confined nature of the 4f orbital[45]. For the adsorbate of 4f atoms, STM studies showed no Kondo resonance. Thus, we consider that the Kondo feature we found is not derived from Dy 4f spin, including cases where the molecule is dissociated and a Dy atom is exposed.

It is worth mentioning that the reverse process is more complicated than the forward process. In our case, the electron-injection process for the backward transformation of MC→SP and MC-DyL(hfac)$_2$→SP-DyL(hfac)$_2$ failed. As discussed above and shown in SI, the conversion from MC to SP states is through the cis-MC state. Thus, the rate of the backward process from MC to SP molecule is determined by the energy barrier between the trans-MC (stable MC state) to cis-MC states, whose energy varies depending on the neighboring conditions like solution, vacuum, and on-surface[42]. On a semi-metallic Bi surface with a low density of states near the Fermi level, it was reported that a bidirectional ring-opening and ring-closing reaction between SP and MC[29]. The difference from our case can be due to the relaxation time of the excited state of MC, as claimed in the report. At the same time, the difference in the bonding/electronic configurations on Bi(110) and Au (111) should contribute to the observed differences[6, 27, 29]. For the MC-DyL(hfac)$_2$ case, the strong affinity between dysprosium cation and the phenolate oxygen in the MC-DyL(hfac)$_2$ complex inhibits the returning process[46]. Since a reversible transformation is critical for applications, the mechanism should be examined in more detail in the future.

Conclusions

In the present work, we show that the tunneling electrons triggered conformational changes of SP to MC and SP-DyL(hfac)$_2$ to MC-DyL(hfac)$_2$ were successfully implemented with tunneling electrons injection. The isomerization process was confirmed by detecting the Kondo resonance. The experimentally observed remarkable zero-bias conductance peak near the Fermi level was ascribed to the intrinsic unpaired spin of conjugated π-radical orbital of MC and MC-DyL(hfac)$_2$ radical, which were theoretically corroborated by DFT calculations. In contrast, the non-electron excited SP and SP-DyL(hfac)$_2$ should not show such enhanced features at the Fermi level, which can be attributed to the fact that the π-electron system at both ends of the spiro$_{C\text{-}O}$ bond are

View Article Online
DOI: 10.1039/D3TC02513F

independent of each other and have no interaction between them. This work will promote the development of single-molecule magnets by enveloping new types of single-molecule magnets with novel designs and performance. On the other hand, it might facilitate the realization of quantum information coding by using the different spin states of photochromic functionalized single-molecule magnets.

Author Contributions

J.H. and T.K. conceived the project; J.H. performed the measurements; J.H., T.K. and L.S. carried out the data analysis; D.L. and Z.W. performed simulations to optimize the measurements; L.N. and S.R. made the samples; J.H. and T.K. wrote the paper. All authors discussed the manuscript.

Conflicts of interest

The authors declare no competing interests.

Acknowledgments

This work was supported in part by Grant-in-Aid for Scientific Research (S) (No.19H05621) (for TK). D.L. acknowledges the HPC resources from CALMIP (Grant 2023-[P21023]).

References

1. Y. Ma, Y. Wen and Y. Song, *J. Mater. Chem.*, 2011, **21**, 3522-3533.

2. V. V. Albert, J. P. Covey and J. Preskill, *Phys. Rev. X*, 2020, **10**, 1-46.

3. A. Urtizberea, E. Natividad, P. Alonso, M. A. Andres, I. Gascon, M. Goldmann and O. Roubeau, *Adv. Funct. Mater.*, 2018, **28**, 1-15.

4. F. Gao, D. Li, C. Barreteau and M. Brandbyge, *Phys. Rev. Lett.*, 2022, **129**, 027201.

5. A. Urtizberea, E. Natividad, P. J. Alonso, L. Pérez-Martínez, M. A. Andrés, I. Gascón, I. Gimeno, F. Luis and O. Roubeau, *Mater. Horizons*, 2020, **7**, 885-897.

View Article Online
DOI: 10.1039/D3TC02513F

6. R. Klajn, *Chem. Soc. Rev.*, 2014, **43**, 148-184.

7. C. P. Collier, G. Mattersteig, E. W. Wong, Y. Luo, K. Beverly, J. Sampaio, F. M. Raymo, J. F. Stoddart* and J. R. Heath*, *Science*, 2000, **289**, 1172-1175.

8. M. L. Bocquet, N. Lorente, R. Berndt and M. Gruber, *Angew. Chem. Int. Ed.*, 2019, **58**, 821-824.

9. D. J. Choi and N. Lorente, in *Handbook of Materials Modeling*, ed. S. Yip, Springer Cham, 2018, pp. 1-32.

10. S. Karan, N. Li, Y. Zhang, Y. He, I. P. Hong, H. Song, J.-T. Lü, Y. Wang, L. Peng, K. Wu, G. S. Michelitsch, R. J. Maurer, K. Diller, K. Reuter, A. Weismann and R. Berndt, *Phys. Rev. Lett.*, 2016, **116**, 027201.

11. Y. He, N. Li, I. E. Castelli, R. Li, Y. Zhang, X. Zhang, C. Li, B. Wang, S. Gao, L. Peng, S. Hou, Z. Shen, J.-T. Lü, K. Wu, P. Hedegård and Y. Wang, *Phys. Rev. Lett.*, 2022, **128**, 236401.

12. A. Köbke, F. Gutzeit, F. Röhricht, A. Schlimm, J. Grunwald, F. Tuczek, M. Studniarek, D. Longo, F. Choueikani, E. Otero, P. Ohresser, S. Rohlf, S. Johannsen, F. Diekmann, K. Rossnagel, A. Weismann, T. Jasper-Toennies, C. Näther, R. Herges, R. Berndt and M. Gruber, *Nat. Nanotechnol.*, 2020, **15**, 18-21.

13. P. Wahl, L. Diekhoner, M. A. Schneider, L. Vitali, G. Wittich and K. Kern, *Phys. Rev. Lett.*, 2004, **93**, 176603.

14. A. Dilullo, S. H. Chang, N. Baadji, K. Clark, J. P. Klockner, M. H. Prosenc, S. Sanvito, R. Wiesendanger, G. Hoffmann and S. W. Hla, *Nano. Lett.*, 2012, **12**, 3174-3179.

15. A. J. Heinrich, C. P. Lutz and D. M. Eigler, *Science*, 2004, **306**, 466-469.

16. N. Darwish, A. C. Aragones, T. Darwish, S. Ciampi and I. Diez-Perez, *Nano. Lett.*, 2014, **14**, 7064-7070.

17. P. Selvanathan, G. Huang, T. Guizouarn, T. Roisnel, G. Fernandez-Garcia, F. Totti, B. Le Guennic, G. Calvez, K. Bernot, L. Norel and S. Rigaut, *Chem. Eur. J.*, 2016, **22**, 15222-15226.

18. M. M. Paquette, R. A. Kopelman, E. Beitler and N. L. Frank, *Chem. Commun.*, 2009, 5424-5426.

19. M. M. Paquette, B. O. Patrick and N. L. Frank, *J. Am. Chem. Soc.*, 2011, **133**, 10081-10093.

20. G. Kresse and D. Joubert, *Phys. Rev. B*, 1999, **59**, 1758-1775.

21. G. Kresse and J. Furthmuller, *Phys. Rev. B*, 1996, **54**, 11169-11186.

22. G. Kresse and J. Furthmuller, *Comput. Mater. Sci*, 1996, **6**, 15-50.

View Article Online
DOI: 10.1039/D3TC02513F

23. J. P. Perdew, K. Burke and M. Ernzerhof, *Phys. Rev. Lett.*, 1996, **77**, 3865-3868.

24. P. Giannozzi, S. Baroni, N. Bonini, M. Calandra, R. Car, C. Cavazzoni, D. Ceresoli, G. L. Chiarotti, M. Cococcioni, I. Dabo, A. Dal Corso, S. de Gironcoli, S. Fabris, G. Fratesi, R. Gebauer, U. Gerstmann, C. Gougoussis, A. Kokalj, M. Lazzeri, L. Martin-Samos, N. Marzari, F. Mauri, R. Mazzarello, S. Paolini, A. Pasquarello, L. Paulatto, C. Sbraccia, S. Scandolo, G. Sclauzero, A. P. Seitsonen, A. Smogunov, P. Umari and R. M. Wentzcovitch, *J. Condens. Matter. Phys.*, 2009, **21**, 1-19.

25. A. D. Becke, *J. Chem. Phys.*, 1993, **98**, 5648-5652.

26. F. Wu, J. Liu, P. Mishra, T. Komeda, J. Mack, Y. Chang, N. Kobayashi and Z. Shen, *Nat. Commun.*, 2015, **6**, 7547.

27. M. Piantek, G. Schulze, M. Koch, K. J. Franke, F. Leyssner, A. Kruger, C. Navıo, J. Miguel, M. Bernien, M. Wolf, W. Kuch, P. Tegeder and J. I. Pascual, *J. Am. Chem. Soc.*, 2009, **131**, 12729-12735.

28. T. Huang, A. D. Zhao, H. Q. Wang, B. Wang, J. L. Yang and J. G. Hou, *J. Am. Chem. Soc.*, 2007, **129**, 3857-3862.

29. G. Schulze, K. J. Franke and J. I. Pascual, *Phys. Rev. Lett.*, 2012, **109**, 1-5.

30. S. I. Kuroda, M. Sugi and S. Iizima, *Thin Solid Films*, 1983, **99**, 21-24.

31. J. Kondo, *Phys Rev*, 1968, **169**, 437-440.

32. J. Kondo, *Prog. Theor. Phys.*, 1964, **32**, 37-49.

33. A. D. Zhao, Q. X. Li, L. Chen, H. J. Xiang, W. H. Wang, S. Pan, B. Wang, X. D. Xiao, J. L. Yang, J. G. Hou and Q. S. Zhu, *Science*, 2005, **309**, 1542-1544.

34. L. Gao, W. Ji, Y. B. Hu, Z. H. Cheng, Z. T. Deng, Q. Liu, N. Jiang, X. Lin, W. Guo, S. X. Du, W. A. Hofer, X. C. Xie and H. J. Gao, *Phys. Rev. Lett.*, 2007, **99**, 106402.

35. N. Tsukahara, K. I. Noto, M. Ohara, S. Shiraki, N. Takagi, Y. Takata, J. Miyawaki, M. Taguchi, A. Chainani, S. Shin and M. Kawai, *Phys. Rev. Lett.*, 2009, **102**, 167203.

36. E. Minamitani, N. Tsukahara, D. Matsunaka, Y. Kim, N. Takagi and M. Kawai, *Phys. Rev. Lett.*, 2012, **109**, 086602.

37. J. Hou, Y. Wang, K. Eguchi, C. Nanjo, T. Takaoka, Y. Sainoo, R. Arafune, K. Awaga and T. Komeda, *Commun. Chem.*, 2020, **3**, 36.

38. T. Komeda, H. Isshiki, J. Liu, Y. F. Zhang, N. Lorente, K. Katoh, B. K. Breedlove and M. Yamashita, *Nat. Commun.*, 2011, **2**, 217.

View Article Online
DOI: 10.1039/D3TC02513F

39. J. T. Li, W. D. Schneider, R. Berndt and B. Delley, *Phys. Rev. Lett.*, 1998, **80**, 2893-2896.

40. U. Fano, *Phys. Rev.*, 1961, **124**, 1866-1878.

41. A. E. Miroshnichenko, S. Flach and Y. S. Kivshar, *Rev. Mod. Phys.*, 2010, **82**, 2257-2298.

42. J. T. C. Wojtyk, A. Wasey, P. M. Kazmaier, S. Hoz and E. Buncel, *J. Phys. Chem. A*, 2000, **104**, 9046-9055.

43. R. Bhuvaneswari, V. Nagarajan and R. Chandiramouli, *Chem. Phys. Lett.*, 2018, **691**, 37-43.

44. P. B. Markworth, B. D. Adamson, N. J. Coughlan, L. Goerigk and E. J. Bieske, *Phys. Chem. Chem. Phys.*, 2015, **17**, 25676-25688.

45. M. Steinbrecher, A. Sonntag, M. d. S. Dias, M. Bouhassoune, S. Lounis, J. Wiebe, R. Wiesendanger and A. A. Khajetoorians, *Nat. Commun.*, 2016, **7**, 10454.

46. P. Selvanathan, V. Dorcet, T. Roisnel, K. Bernot, G. Huang, B. Le Guennic, L. Norel and S. Rigaut, *Dalton Trans.*, 2018, **47**, 4139-4148.

Supporting Information

Spin State Manipulation of Spiropyran (SP) and Dy Complex with SP Ligand Molecules on Au (111) by Scanning Tunneling Microscopy

Jie Hou[1], Dongzhe Li[2], Lucie Norel[3], Stéphane Rigaut[3], Zhipeng Wang[4], Lei Shan[1], Tadahiro Komeda[4,5*]*

[1]Key Laboratory of Structure and Functional Regulation of Hybrid Materials of Ministry of Education, Institutes of Physical Science and Information Technology, Anhui University, Hefei 230601, China

[2]CEMES, Université de Toulouse, CNRS, 29 rue Jeanne Marvig, F-31055 Toulouse, France

[3]Institute of Chemical Sciences of Rennes (ISCR), UMR 6226 CNRS, University of Rennes 1, Rennes Cedex, France

[4]Institute of Multidisciplinary Research for Advanced Materials (IMRAM, Tagen), Tohoku University, 2-1-1, Katahira, Aoba-Ku, Sendai 980-0877, Japan

[5]Center for Spintronics Research Network, Tohoku University, 2-1-1 Katahira, Aoba-ku, Sendai 980-8577, Japan

Table of contents

1. Energy diagram of the isomerization between SP and MC

We consider these activation energies in the energy diagram for the conversion between the SP and MC molecules. It was reported in the previous reports for the SP-MC conversion in the solution that the MC molecule is in the *trans*-MC state which is converted into the SP molecule through the transition *cis*-MC state as illustrated in **Figure S1**[1], in which the existence of the transition state was confirmed by the ultra-fast optical measurement. Thus, the activation energy from the MC to SP molecule should be the energy difference between the *trans*- and *cis*-MC. It is reported that the isomerization takes place with a dihedral angle rearrangement and conquering a steric hindrance for the configuration change[1]. In this process, the dihedral angles should be rotated: α 180 → 90, β 180 → 0, and γ 180 → 0. The rotation is schematically illustrated in **Figure S1** by arrows. Two types of thermal decay rate from MC to SP were confirmed; activation energies are 71.5 kJ/mol and 90.0 kJ/mol for the rapid-decay and slow-decay components, respectively[2].

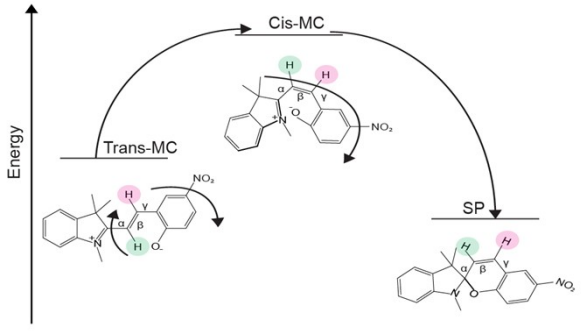

Figure S1 Potential energy diagram for the conversion of MC to SP.

2. Temperature-dependent zero-bias-peak variation to verify the Kondo resonance

The relation between the width of the peak (2Γ) and the sample temperature (T) should be connected with eq (1).

$$2\Gamma = \sqrt{(\pi k_B T)^2 + 2(k_B T_K)^2} \qquad (1),$$

where T_K is the Kondo temperature, and k_B is the Boltzmann constant[3]. We have measured the MC molecule sample for the sample temperature of 4.7 (plot I) to 64 K (plot IV) as shown in **Figure S2 (a)**. The fit results of the peak width are plotted in **Figure S2 (b)** with corresponding error bars. The points can be fit well with using eq (1) with the corresponding T_K of ~ 110 K.

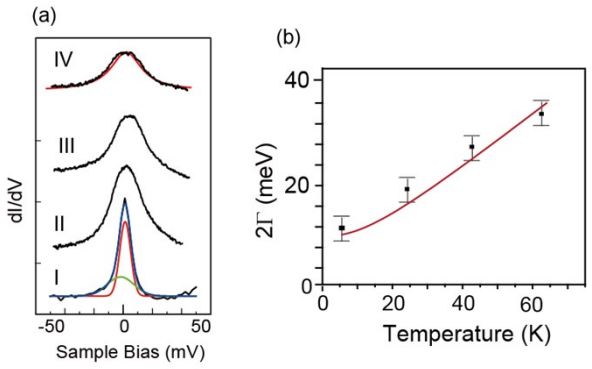

Figure S2 (a) Temperature dependence of the zero bias peak measured in the temperature region of 4.7–64 K for the MC molecule. The solid curves are the results of fitting using the Fano function depicted in eq. (1). (b) Peak width (2Γ) vs temperature plot with error bars. The solid curve indicates the fitted curve using the eq. (1).

3. SIMS analysis of SP-DyL(hfac)$_2$ molecule transferred onto Au (111) by drop-cast

The sample molecule transferred on Au/mica substrate was examined using the mass spectrometer. The solution was drop-casted onto Au/mica substrate, dried with nitrogen gas, and finally transferred to the UHV chamber for mass examination. We employed time-of-flight secondary ion mass spectrometry (ToF-SIMS) using the machine of ION-

TOF SIMS 5 (ION-TOF GmbH). A 25 keV Bi_3^+ ion was used as a primary ion, which hits the target at an angle of 45°. The lateral resolution was approximately 1 μm, and the mass resolution (m/Δm) was 4000. The pulsed target current was 0.1 pA. Analysis areas were within 50×50 μm^2.

Figure S3 shows the result of the area for the intact molecule. The main peak at m/z= 1111.7 should correspond to $C_{42}H_{33}DyF_{12}N_5O_7$ for the ^{164}Dy among natural abundance. The total mass should be calculated as 1111.7. The rest of the peaks are natural abundance of Dy (^{161}Dy, ^{162}Dy, ^{163}Dy and ^{164}Dy are known to have higher proportion, in addition to the attachment and detachment of H atoms.

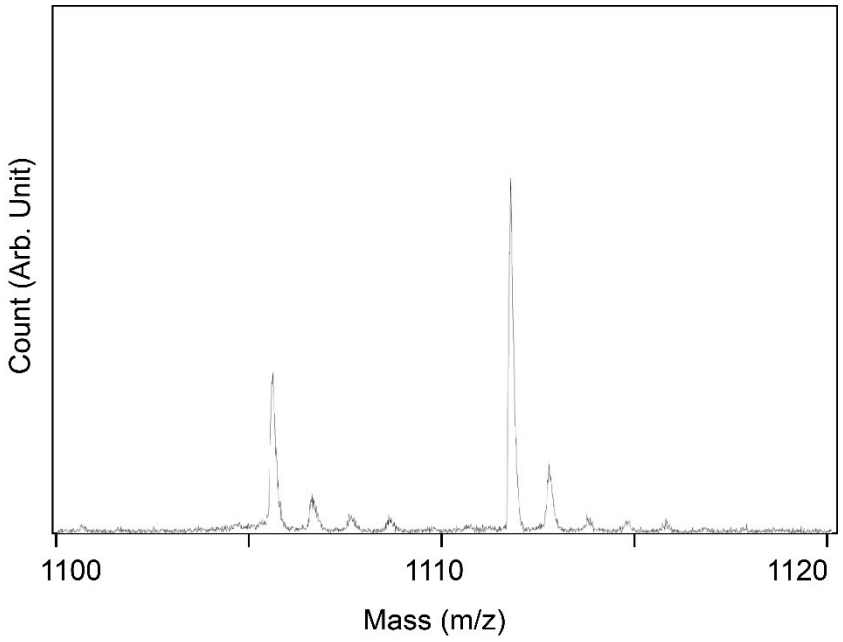

Figure S3 ToF-SIMS spectrum obtained for the drop-casted sample (substrate is Au on mica). The main peak appears at m/z=1111.7.

Reference

1. J. T. C. Wojtyk, A. Wasey, P. M. Kazmaier, S. Hoz and E. Buncel, *J. Phys. Chem. A*, 2000, **104**, 9046-9055.

2. M. S. A. Mamun, Y. Sainoo, T. Takaoka, H. Waizumi, Z. Wang, M. I. Alam, A. Ando, R. Arafune and T. Komeda, *Phys. Chem. Chem. Phys.*, 2021, **23**, 27273-27281.

3. K. Nagaoka, T. Jamneala, M. Grobis and M. F. Crommie, *Phys. Rev. Lett.*, 2002, **88**, 077205.